

A COMPARATIVE STUDY OF THE AERODYNAMIC CHARACTERISTICS OF FOUR CONFIGURATIONS

Kai You[1], Rongbo Zhu[1], Zhenli Chen[1,2*]

[1]School of Aeronautics, Northwestern Polytechnical University, Xi'an 710072, China

[2]National Key Laboratory of Aircraft Configuration Design, Xi'an 710072, China

Abstract

With superior aerodynamic performance and stealth capability, flying-wing configurations are preferred configurations for future unmanned combat air vehicles (UCAVs), which are well adapted for high-risk missions such as penetration, air defense suppression and high-value target strike. These configurations generally adopt moderate aspect ratios and leading-edge sweep angles. However, most flying-wing designs encounter the problem of nonlinear pitch-up of pitching moment, which reduces the usable maximal lift coefficient and impairs longitudinal stability at high angles of attack. The effects of planform and sectional leading-edge radius on the pitch-up characteristics of flying-wing UCAVs derived from a baseline SACCON configuration are studied by using a computational fluid dynamics method in present work. The associated flow mechanisms of moment pitch-up are analyzed. When sectional airfoils are fixed and the leading-edge sweep angle is increased to alter the planform, the pitch-up onset is effectively delayed. Physically, a larger leading-edge sweep restrains the inboard migration of vortices and weakens the adverse suction aft of the moment reference point, thereby postponing the nonlinear variation of pitching moment. For configurations with identical sectional airfoils and leading-edge sweep angles, extending the trailing-edge shape cannot fully eliminate the pitch-up, but can eliminate the abrupt pitch break. However, the pitching moment slope still rises markedly, which is caused by the rapid forward movement of the outer-wing vortex. In contrast, extending the trailing-edge shape and increasing the sectional leading-edge radius can completely suppresses nonlinear pitch-up. The enlarged leading-edge radius sustains a large attached-flow region over the wing, weakens both apex and outer-wing vortices, and prevents vortex coalescence. As a result, the pitching moment varies steadily over a wide range of angles of attack. In conclusion, both planform and sectional airfoils exert remarkable influences on UCAV pitch-up, and their coordinated matching is therefore an essential option in flying-wing configuration design.

Keywords: CFD; pitch-up; planform; SACCON; UCAV;

1. Introduction

Flying-wing Unmanned Combat Air Vehicles (UCAVs) face a prominent pitch-up problem of longitudinal pitching moment, which limits their low-speed take-off and landing capabilities.

Both planform and sectional airfoil profiles exert remarkable effects on the pitch-up behavior of pitching moment. The influences of planform are primarily embodied in its aspect ratio AR and the quarter-chord sweep angle $\Lambda_{1/4}$, as shown in Fig. 1. Configurations having $AR \cdot \tan\left|\Lambda_{1/4}\right| < 2.6$ often display pitch-down characteristics, whereas those having $AR \cdot \tan\left|\Lambda_{1/4}\right| > 3.0$ tend to exhibit pitch-up characteristics[1].

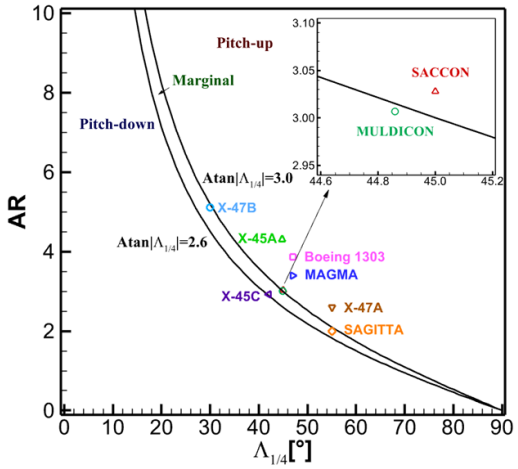


Fig. 1 – Possible moment characteristics corresponding to UCAV planform

To explore the fundamental mechanisms behind pitch-up phenomena of UCAVs with moderate leading-edge sweep and moderate aspect ratios, extensive experimental and numerical investigations on the SACCON flying-wing UCAV configuration have revealed that its prominent nonlinear aerodynamic characteristics are dominated by complex interactions of multiple vortex systems [2]-[4]. The wingtip vortex of SACCON is positioned behind the center of gravity, and the vortex lift it generates initially produces a nose-down pitching moment. As the angle of attack increases, this vortex gradually moves forward and experiences vortex breakdown in the region aft of the center of gravity. This flow phenomenon triggers an abrupt pitch-up at approximately 16°. Prior numerical simulations show good agreement with experimental data at angles of attack below 15°, whereas the predictive accuracy degrades for post-stall flow fields, which is mainly attributed to the inherent limitations of existing turbulence models [5]-[6].

To suppress the undesirable nonlinear pitch-up behavior, a series of modified configurations have been developed via planform and airfoil modifications. The MULDICON configuration adjusts trailing-edge shape and sectional airfoils based on the SACCON configuration [7]-[9]. This design delays flow separation and extends the range of usable lift by maintaining attached flow over the wing surface. Nevertheless, its non-parallel leading and trailing edges inevitably compromise the stealth performance. The SAGITTA configuration adopts a large leading-edge sweep and low aspect ratio, which effectively eliminates pitch-up phenomena under low-speed conditions [10]-[12]. The MAGMA UCAV further mitigates longitudinal instability by combining geometric modification with Coanda-effect circulation control technology [12].

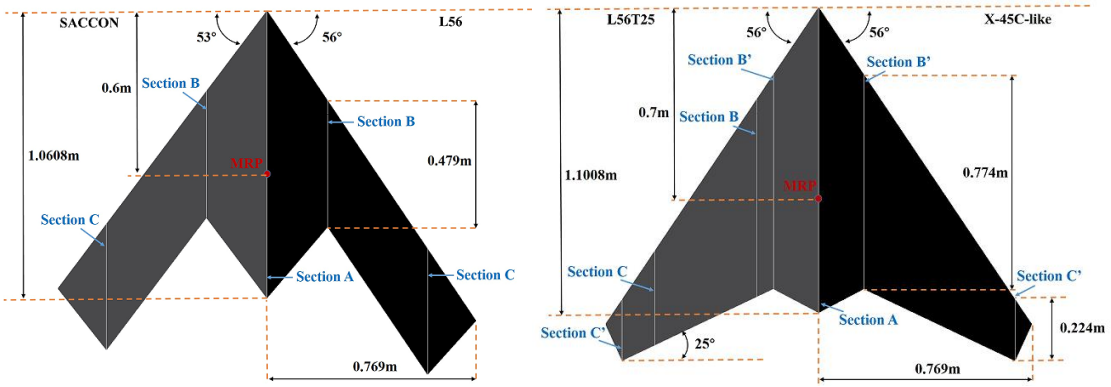
It has been validated in relevant vortex flow studies that not only planform but also sectional airfoils and leading-edge contour radii exert decisive impacts on vortex evolution and pitching moment characteristics. The leading-edge radius directly impacts the onset of flow separation. A larger leading-edge radius can delay separation and maintain attached flow over a wider angle-of-attack, yet excessively large leading-edge radius will deteriorate high-speed aerodynamic performance and stealth. In practice, it is technically challenging to sustain fully attached flow up to high angles of attack while balancing multi-performance constraints. In summary, to develop a high-performance flying-wing UCAV, it is necessary to jointly design both planform and sectional airfoils, enabling the UCAV to combine excellent cruise aerodynamic performance with reliable low-speed takeoff and landing characteristics.

To explore the influences of planform and sectional airfoils on aerodynamic performance, four configurations are established in the present work. Taking the baseline SACCON configuration as the reference, three derived configurations, namely L56, L56T25 and X-45C-like, are developed for comparative analysis. Numerical studies are carried out to investigate their pitch-up characteristics and the corresponding flow mechanisms. The details of the configurations and the adopted numerical methods and their validation are presented in Section 2. A comprehensive analysis of the obtained results and the underlying physical mechanisms are discussed in detail in Section 3. Finally, the main conclusions are given.

2. Models, Computational Method and its Validation

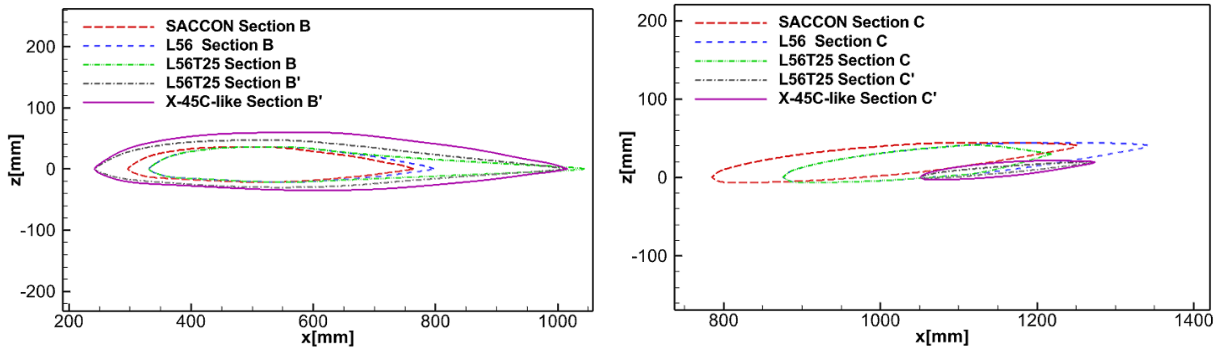
2.1 Models

The SACCON configuration used in this work has the same geometric dimensions to the low-speed wind tunnel model. The L56 configuration employs the same airfoils at sections A, B and C, as well as identical chord lengths, span and twist distributions as SACCON, with its leading-edge sweep angle increased to 56°. L56T25 fully retains the forward geometry of L56, and only modifies the trailing-edge section to match the planform of a X-45C-like configuration having trailing-edge swept angle of 25°. The leading-edge radius distribution of L56T25 also remains the same with that of L56. For the X-45C-like model, the airfoils at sections B' and C' correspond respectively to those at sections B and C of SACCON and L56. The planforms of the four configurations are presented in Fig. 2, and the airfoil comparisons at sections B, B', C and C' are given in Fig. 3. The reference chord is 0.479 m for SACCON [6] and L56, while L56T25 and the X-45C-like configuration having an aerodynamic mean chord of 0.684 m. The reference area is 0.77 m^2 for SACCON [6] and L56, and it is 0.86 m^2 for L56T25 and the X-45C-like configurations.



(a) SACCON and L56 (b) L56T25 and X-45C-like

Fig. 2 – Comparison of four configurations



(a) section B (y=222mm) and B' (y=163mm) (b) section C (y=582mm) and C' (y=709mm)

Fig. 3 – Comparison of airfoils at section B, B' and C, C'

2.2 Computational Method

In the present work, a Reynolds-averaged Navier–Stokes (RANS) flow solver is adopted to conduct the numerical simulations. It solves the compressible three-dimensional RANS equations using a finite-volume formulation.

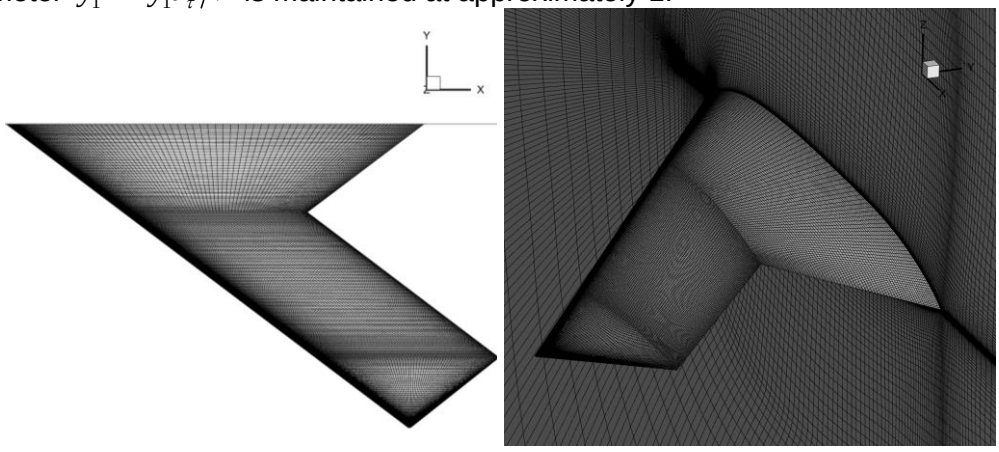
The one-equation Spalart–Allmaras (SA) turbulence model is applied for turbulence closure [13]. Fully turbulent flow conditions are assumed in all simulations to eliminate the interference of transition effects. For the boundary conditions, the characteristic non-reflecting boundary conditions are imposed at the far-field boundaries to avoid non-physical wave reflections that could disturb the flow field solution. Symmetry boundary conditions are applied on the symmetry plane of the computational domain, taking advantage of the symmetric nature of the present flying-wing configurations. On all solid wall surfaces, adiabatic no-slip boundary conditions are enforced to model the viscous interaction between the flow and the wing surface.

The current simulations have been performed using a second-order backward Euler scheme. For

spatial discretization, the convective terms are discretized using a second-order total variation diminishing (TVD) scheme based on a multi-dimensional interpolation framework[14], which is capable of capturing the strong gradients in the vortex cores without introducing excessive numerical dissipation. The viscous terms, on the other hand, are treated with a second-order central differencing scheme to ensure accurate prediction of the viscous stresses in the boundary layer and shear layers.

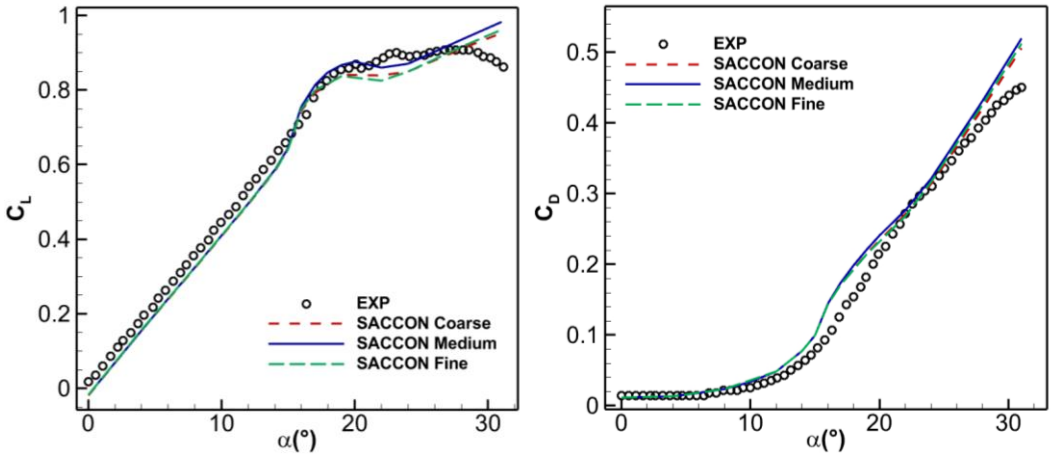
2.3 Method's validation

To validate the numerical approach and examine grid convergence characteristics, numerical simulations of the SACCON configuration were performed under identical flow conditions as the corresponding wind tunnel tests, with the Mach number set to $M = 0.15$ and Reynolds number equal to $Re = 1.6 \times 10^6$ [2]. The baseline grid is shown in Fig. 4. The baseline computational grid is presented in Fig. 4. Based on this baseline mesh, grid refinement was implemented along both the chordwise and spanwise directions. Further refinement is conducted for the boundary-layer region and flow domains where vortical structures develop, forming the fine grid. In contrast, the coarse grid is generated by coarsening the mesh in the same way. For baseline grid, the nondimensional boundary-layer parameter $y_1^+ = y_1 u_\tau / \nu$ is maintained at approximately 1.

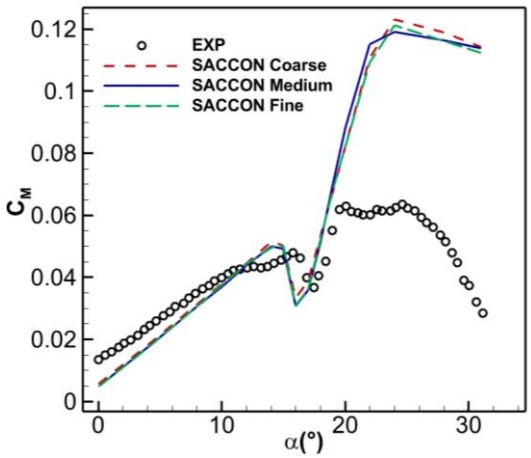


(a) Top view (b) Rear view

Fig. 4 – Structured grid views



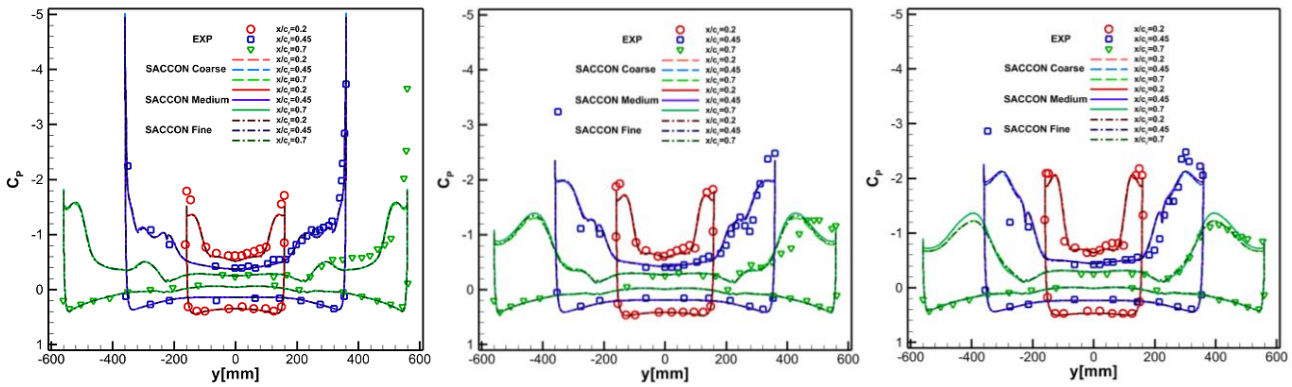
(a) Lift coefficient (b) Drag coefficient



(c) Pitching moment coefficient

Fig. 5 – Comparisons of longitudinal aerodynamic forces and moments

The coarse, medium and fine grids have 7 million, 14 million, and 21 million cells, respectively. The SACCON results calculated with three grid resolutions are compared with the experimental results, as shown in Fig. 5. At angles of attack below 18°, the results of the three grid resolutions are nearly identical in lift, drag, and pitching moment. At angles above 18°, the three grids may produce slight differences due to the prediction of vortex breakdown locations. For angles of attack below 15°, the slope of the lift curve obtained by the RANS is in good agreement with the experimental data. However, the absolute lift coefficient is systematically lower about 0.03, which may be due to the difference between the reconstructed and the experimental configuration. As the angle of attack further increases, the RANS method is unable to accurately reproduce the strong nonlinear lift growth characteristic in the experiment. The predicted zero-lift drag is in good agreement with that of experiment. However, near the angle of attack corresponding to the pitch-up point, the drag is about 0.044 higher than the experimental results, indicating that the current model has large discrepancies in predicting drag in the regime of vortex dominated flow. The predicted pitching-moment coefficient is quite different with that of experiment. The predicted pitch-up angle of attack is about 1.5° earlier than that of experiment. The predicted slope of the pitching moment is larger than that of the experiment when the angle of attack is below 12°. The present numerical results are consistent with other numerical results obtained using RANS [15]. The discrepancy may be caused by the fact that the sting is not included, which can play an important role in predicting the pitching moment [15].



(a) $\alpha = 15^\circ$ (b) $\alpha = 17^\circ$ (c) $\alpha = 19^\circ$

Fig. 6 – Comparisons of sectional pressures at different angles of attack

To further show the prediction capability of the numerical method, the surface pressure distributions at different cross-section are compared with that of experiments in Fig. 6 at three angles of attack near the pitch-up. With increasing angle of attack, the apex vortex and outer wing vortex become stronger, which generates strong suction, and their onset moves inboard.

At an angle of 15°, at $x/c_r = 0.2$, the predicted pressure at the leading edge is lower than the

corresponding experimental result. At $x/c_r = 0.45$, two distinct vortex cores are observed near 240 mm and 300 mm, with both the positions and pressure values for the inner and outer vortex closely aligning with the experimental data. At $x/c_r = 0.7$, all three grid resolutions reveal clear inboard and outboard vortices, however, these features are not present in the experimental results.

When the angle of attack reaches 17° at $x/c_r = 0.2$, the predicted pressure remains lower than the experimental results; however, the error has decreased. Additionally, the vortex core shifts inboard, which aligns with the experimental observations. At $x/c_r = 0.45$, the strength of the outer vortex in the numerical results is lower than that observed in the experiment. Conversely, at $x/c_r = 0.7$, the strength of the outer vortex in the numerical results is nearly equivalent to that in the experiment, although the core has shifted inward by 60 mm.

At an angle of 19° and at $x/c_r = 0.2$, the predicted pressure at the leading edge closely aligns with experimental results; however, the core of the apex vortex at this section is displaced inward by nearly 20 mm compared to the experimental data. At $x/c_r = 0.45$, the core of the outer vortex is positioned similarly to that observed in the experiment, yet the predicted pressure is significantly lower than the experimental values. For $x/c_r = 0.7$, in contrast to findings in other areas, the forecasts for the outer vortex core's position at this specific section demonstrate consistent accuracy across all three grid resolutions, albeit with minor variations in pressure readings that could be ascribed to spatial refinement.

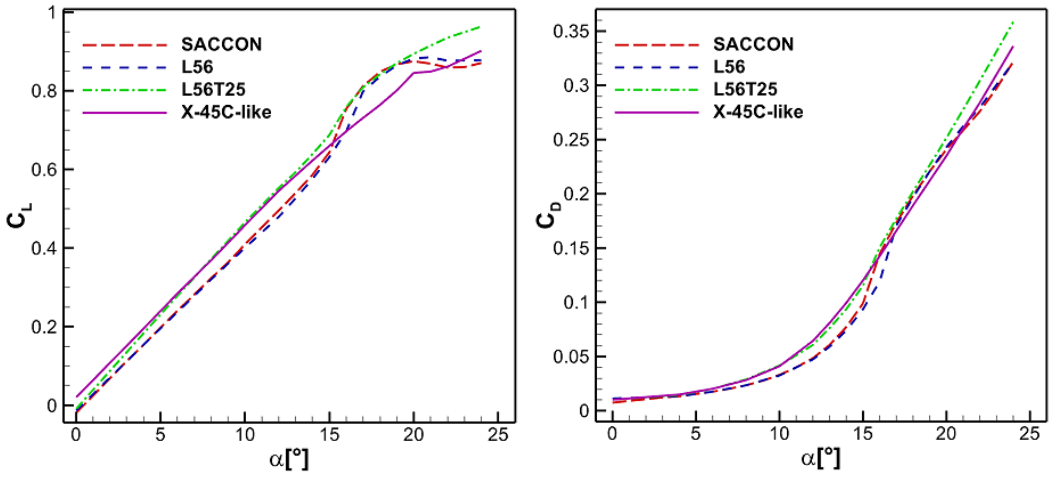
Overall, the RANS method demonstrates reasonable agreement with experimental results at higher angles, but it displays errors in vortex-induced pressure and core location at specific chordwise stations.

Grid convergence is achieved for the three computational grids. The calculated lift, drag and pitching moment coefficients exhibit negligible differences across different resolutions. The linear-region lift-curve slope agrees well with experimental data, and the error in pitch-up onset angle is within 2 degrees. This verifies the reliability of the adopted numerical method. Furthermore, surface pressure distributions predicted by the three grids are nearly identical, and vortex core positions show no obvious deviation, with minor discrepancies only appearing locally due to grid refinement. To reduce computational cost, a 14-million-cell grid is adopted for all subsequent calculations.

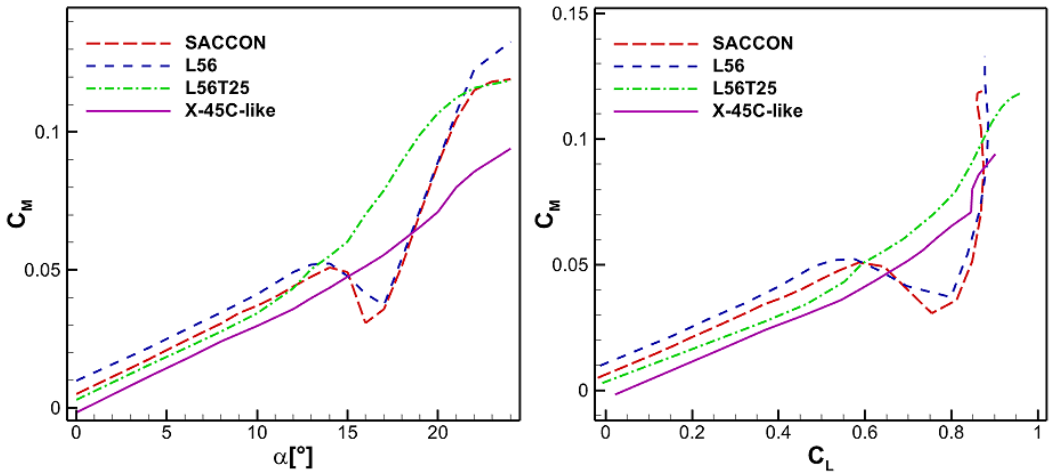
3. Results and Discussions

3.1 Effects of planform and sectional airfoils on Aerodynamic Forces and Moments

To show the planform effects on the aerodynamic characteristics, the aerodynamic forces and moments are firstly compared in Fig. 7.



(a) Lift coefficient (b) Drag coefficient



(c) Pitching moment coefficient (d) Pitching moment coefficient vs. Lift coefficient

Fig. 7 – Comparisons of longitudinal aerodynamic forces and moments

The lift and lift-curve slope show significant planform dependence, as illustrated in Fig. 7(a). The lift increases almost linearly with angle of attack when $\alpha < 10^{\circ}$. For the L56 configuration, its lift is almost the same as that of SACCON, but its lift-curve slope is slightly smaller due to a higher sweptback angle. The lift of X-45C-like is slightly higher than that of all others. The lift of SACCON exhibits a linear, predictable increase, owing to its well-maintained attached flow and orderly pressure distribution at low to medium angles of attack; its maximum lift coefficient is moderate. Beyond approximately 16°, additional vortex lift causes a marked rise in total lift. The lift of L56 performs almost identically to that of SACCON because the aspect ratio is same, while the additional lift of L56T25 is less pronounced, perhaps because its aspect ratio is smaller. In contrast, the lift of X-45C-like does not gain appreciably from nonlinear vortex lift; its lift-curve slope remains reasonably linear with no significant vortex-lift increment up to 20°.

The drag characteristics of the four configurations demonstrate distinct planform dependence, as illustrated in Fig. 7(b). The drag of SACCON and L56 remains low at angles of attack below 15°. As the angle of attack exceeds 15°, where additional vortex lift becomes apparent as shown in Fig. 7(a), the drag of SACCON and L56 increases more steeply, indicating a greater drag caused by vortex penalty. For angles below 20°, the drag of L56 closely resembles that of SACCON, while the drag of L56T25 aligns with that of X-45C-like, confirming that planform primarily dictates the drag trade-off. At angles of attack above 20°, the drag of SACCON and L56 continues to increase more significantly than that of X-45C-like and L56T25, as the former develop stronger vortex systems that enhance lift but also elevate drag.

To facilitate the comparison of the moment behavior among different configurations, the center of gravity of each configuration is adjusted so that the slopes of the pitching moment in the linear region are matched. It can be seen that both the SACCON configuration and the L56 suffer from a pitch-break as shown in Fig. 7(c), but the pitch-up point of L56 is delayed by 1° compare with that of SACCON. But for the X-45C-like and the L56T25, the pitch-break doesn't show on these two configurations, though the nonlinearity of the pitching moment seems to occur earlier. Especially for the L56T25 configuration, the slope of the pitching moment increases significantly at around 14°. By mitigating the abrupt nose-down pitching break, the vehicle can operate more safely and controllably up to its maximum lift capability. In other words, the maximum available lift coefficient increases from 0.6 for the SACCON to at least 0.8 for the X-45C-like, as shown in Fig. 7(d).

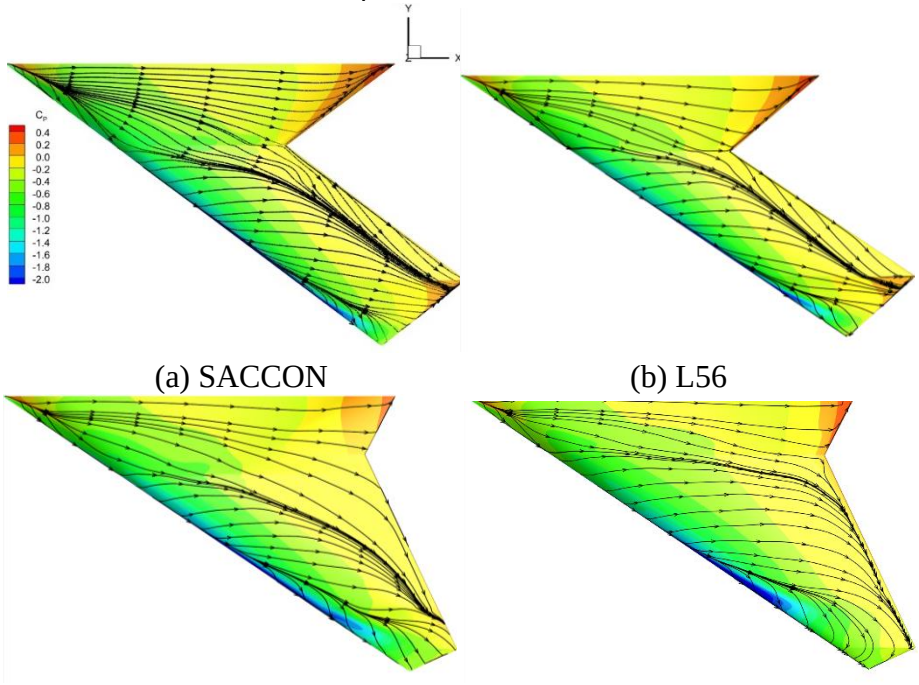
The lift, drag, and pitching moment demonstrate significant dependence on planform characteristics. SACCON and L56 exhibit nearly identical lift up to 20°, although L56 has a slightly lower lift-curve slope due to its increased sweep. Both configurations show a pronounced vortex-lift contribution beyond 15°, leading to a steep rise in drag and a distinct pitch break. For SACCON, the pitch-up occurs around 16°, while L56 experiences this break approximately 1° later. In contrast, X-45C-like and L56T25 exhibit minimal reliance on nonlinear vortex lift; their lift remains linear up to 20°, with X-45C-like achieving a marginally higher lift coefficient. Although their drag is slightly elevated at low

angles, it increases more gradually with incidence, and they do not display a pitch break. However, the nonlinearity of the pitching moment manifests earlier. The absence of an abrupt pitch break enables X-45C-like and L56T25 to operate with enhanced safety and control, elevating the maximum usable lift coefficient from approximately 0.6 for SACCON to 0.8 for X-45C-like.

3.2 Effects of planform and sectional airfoils on pressure distribution

To show the planform effects on surface flow of four configurations, pressure contours and skin limited lines are shown as below. The surface pressure distribution range is [-2.0, 0.4] with blue representing low-pressure areas and red representing high-pressure areas. Combined with the pressure characteristics at key angles of attack, the differences in flow mechanisms are analyzed as follows. During the progression of the angle of attack from 12° to 19°, the surface pressure distributions of the SACCON and X-45C-like configurations exhibit systematic and markedly different evolutionary characteristics.

The interpretation of the flow topology at an angle of attack of 12° is given in Fig. 8, the SACCON configuration shows clear reattachment lines in the leading-edge region of the inner fuselage and at the wingtip leading edge. For SACCON at α =12°, the flow is characterized by distinct reattachment lines and a uniformly moderate pressure field (-1.0 to -0.6) over the attached outer wing. The L56 configuration appears almost identical to SACCON, likely due to the same leading-edge radii distribution. The L56T25 configuration resembles SACCON and L56 in the region upstream of the wingtip-vortex reattachment line, yet it also shows notable differences. L56T25 features a larger aft region on the inner crank and part of the outer crank, unaffected by both the apex vortex and the wingtip vortex, which expands the attached-flow area, and its wingtip vortex begins farther forward; these differences likely arise from pressure-gradient changes associated with the outer-crank and wingtip geometry. The X-45C-like configuration, by contrast, develops a rapidly forming, advancing tip vortex that evolves into an outer vortex while maintaining an attached-flow region over the mid-wing. Its leading-edge pressure, generally between -1.0 and -0.4 away from the vortex origin, indicates a different balance between vortex development and flow attachment.



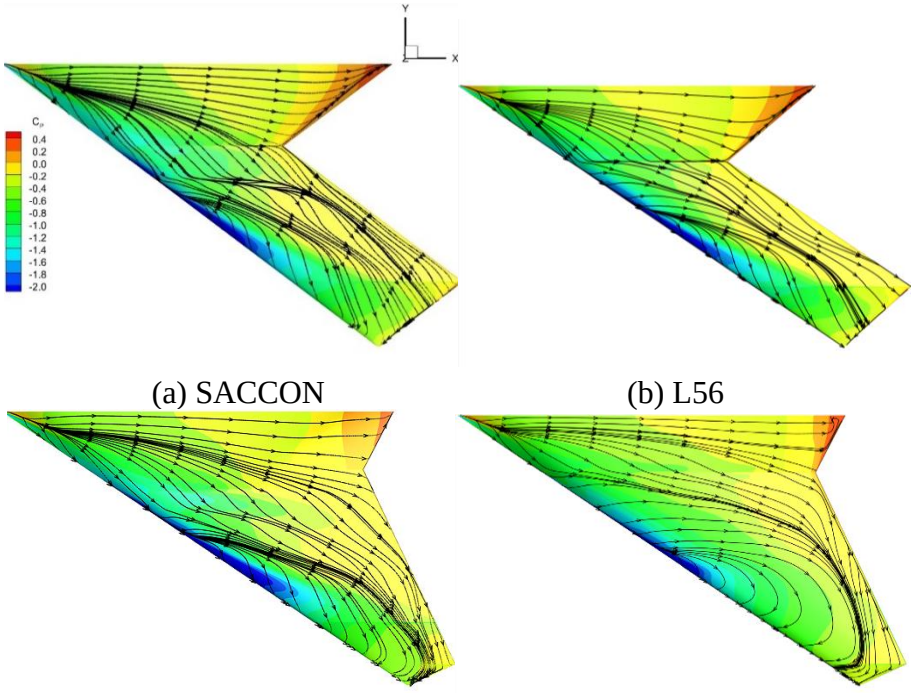
(a) SACCON (b) L56

(c) L56T25 (d) X-45C-like

Fig. 8 – Pressure contours and skin limited lines ($\alpha = 12^{\circ}$)

As the angle of attack increases to 15°, flow separation in the SACCON configuration becomes more pronounced. The wingtip vortex moves inboard and turns into an outer wing vortex, which creates a low-pressure region mainly aft of the center of gravity, and the resulting additional lift there primarily drives the abrupt nose-down moment increase. The separation zone grows rapidly forward from the

trailing edge, producing a large low-pressure area over most of the wingtip as shown in Fig. 9. The pressure distribution becomes more complex, and the limiting streamlines clearly mark the separation envelope. The L56 configuration shows generally the same behavior as SACCON, with one notable difference: no new separation line appears in the mid region near the inner crank. This likely results from the increased sweep angle, which promotes flow attachment and suppresses the formation of a new vortex system. For the SACCON and L56, the wingtip vortex moves inboard and the apex vortex becomes stronger, together generating enough suction at the front part, therefore pitch-up occurs. The L56T25 configuration behaves essentially like L56, with no new separation line at the outer crank, but a pronounced backflow appears in the mid region of the wingtip. The X-45C-like configuration, however, develops a flow regime dominated by strong vortices over the outer wing. Its pressure contours show multiple local extrema, with a pronounced low-pressure zone clearly visible along the leading edge of most mid-wing sections. Outside this region, pressure varies more gradually across the wing surface than in the SACCON configuration, with most areas exhibiting moderate pressure levels.

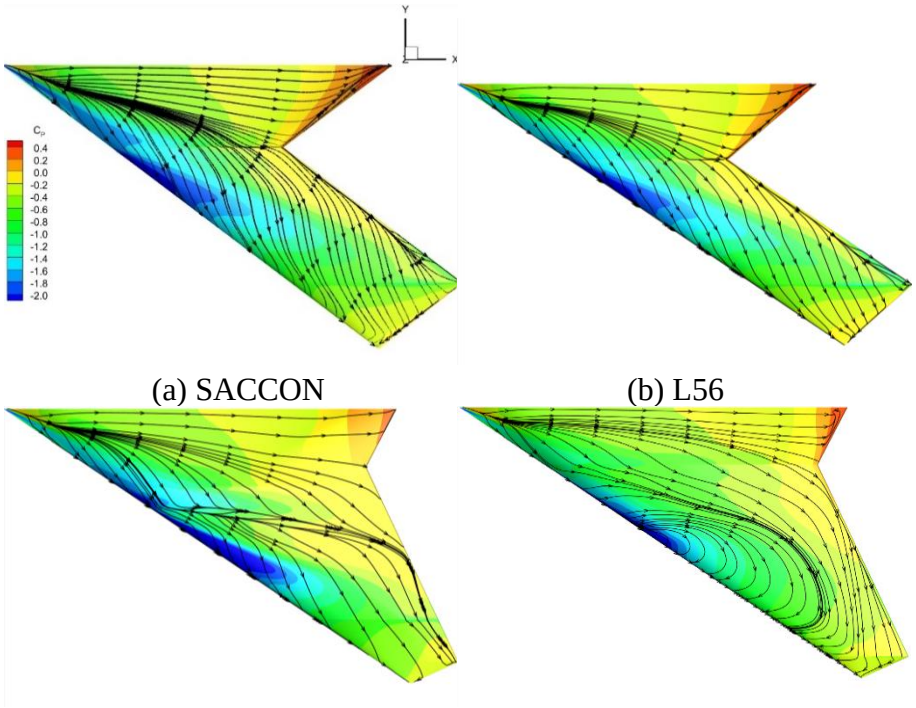


(a) SACCON (b) L56

(c) L56T25 (d) X-45C-like

Fig. 9 – Pressure contours and skin limited lines ($\alpha = 15^{\circ}$)

When the angle of attack reaches 17°, the onset of the outer wing vortex for the SACCON and L56 occurs ahead of the inner crank, and the outer wing vortex appears to merge with the apex vortex as shown in Fig. 10. For L56T25, the onset of the outer wing vortex is at nearly the same position as in the SACCON and L56, but a reseparation forms between the apex vortex and the outer wing vortex. Because the suction generated by the apex vortex becomes large and the onset of the wingtip vortex has moved far ahead of the moment reference point, the slope of the pitching moment for L56T25 increases clearly. For the X-45C-like configuration, the surface pressure distribution is broadly consistent with that at 15°, while the attached-flow region on the leading edge between the apex vortex and the outer wing vortex becomes smaller.

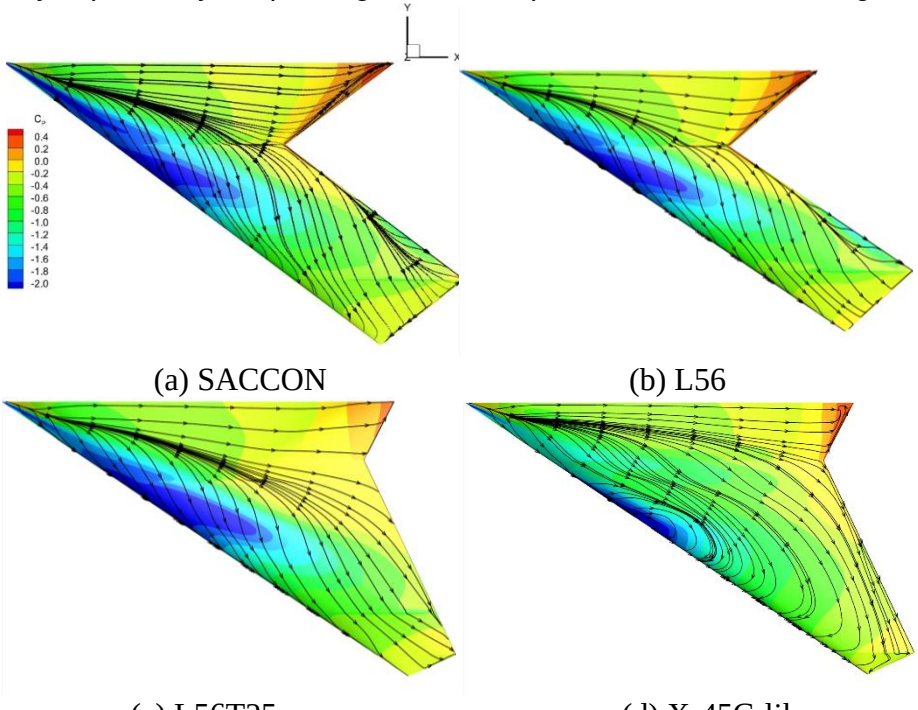


(a) SACCON (b) L56

(c) L56T25 (d) X-45C-like

Fig. 10 – Pressure contours and skin limited lines ($\alpha = 17^{\circ}$)

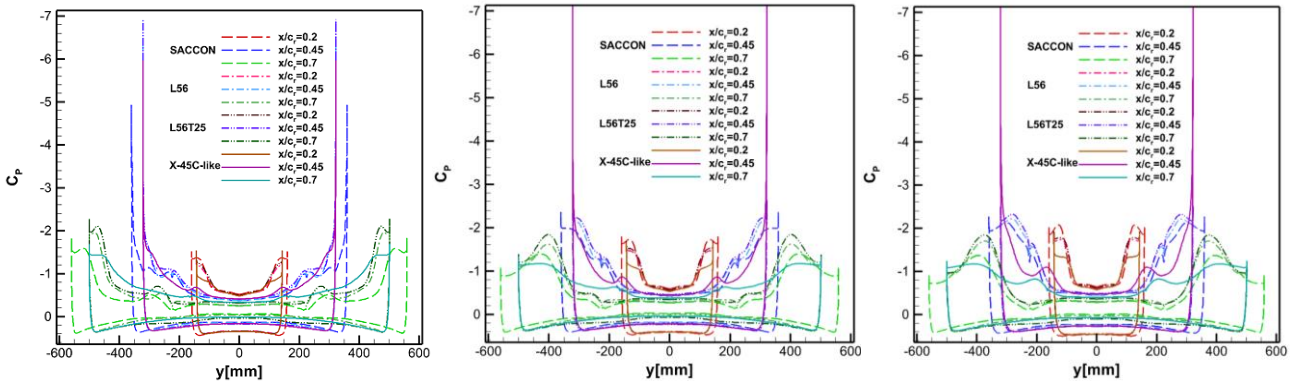
At an angle of attack of 19°, the surface pressure distributions of SACCON, L56, and L56T25 are nearly identical as shown in Fig. 11. The primary distinction is that the increased trailing-edge area of L56T25 preserves attached flow, while the SACCON and L56 show a clear reattachment of the trailing vortex from the inner crank at the outer wing trailing edge. By contrast, the X-45C-like surface pressure exhibits almost no significant change. Compared with L56T25, the suction generated by the apex vortex and the outer wing vortex is not strong and the onset of the outer wing vortex moves slowly, which may explain why the pitching moment slope exhibits no clear change.



(a) SACCON (b) L56

(c) L56T25 (d) X-45C-like

Fig. 11 – Pressure contours and skin limited lines ($\alpha = 19^{\circ}$)



(a) $\alpha = 15^{\circ}$ (b) $\alpha = 17^{\circ}$ (c) $\alpha = 19^{\circ}$

Fig. 12 – Comparisons of sectional pressures at different angles of attack

The comparison of sectional pressures across different configurations at varying angles of attack is illustrated in Fig. 12. At an angle of attack of 15°, the sectional pressure distributions reveal significant longitudinal variations. In the front wing segment at $x/c_r = 0.2$, SACCON demonstrates stronger leading-edge suction on both the left and right sides compared to L56 and L56T25, indicating a more robust apex vortex; conversely, X-45C-like does not exhibit a comparable level of suction. However, the pressure coefficients in the inner regions of all configurations remain nearly identical. In the middle wing segment at $x/c_r = 0.45$, the pressure coefficients vary among configurations, yet none exhibit a pronounced suction peak at the leading edge. Notably, the most significant difference is the presence of two distinct vortex cores between 200 mm and 320 mm for SACCON, whereas the other three configurations display only one vortex core. In the rear wing segment at $x/c_r = 0.7$, SACCON, L56, and L56T25 show a clear leading-edge suction peak, suggesting an influence from the wingtip vortex; the pressure magnitude and vortex-core position differ only slightly among these configurations. Additionally, a suction region appears between 240 mm and 320 mm, indicating the passage of the apex vortex through this section. In contrast, for X-45C-like, the suction generated by the apex vortex is located more inboard near 200 mm and is less pronounced, with the leading-edge suction peak also being weaker than that of the other configurations.

The apex vortex intensifies for the SACCON, L56, and L56T25 configurations at $x/c_r = 0.2$ at an angle of attack of 17°. At $x/c_r = 0.45$, the onset of the wingtip vortex shifts forward toward the midsection, resulting in a more pronounced suction peak at the leading edge compared to previous observations. Furthermore, for all configurations, only one single vortex core is detected near 200 mm. In the rear wing segment at $x/c_r = 0.7$, the forward movement of the wingtip vortex relocates its core inboard to approximately 400 mm, thereby expanding the suction region. Notably, for the X-45C-like, the suction peak of wing tip vortex remains significantly weaker than that of the other three configurations.

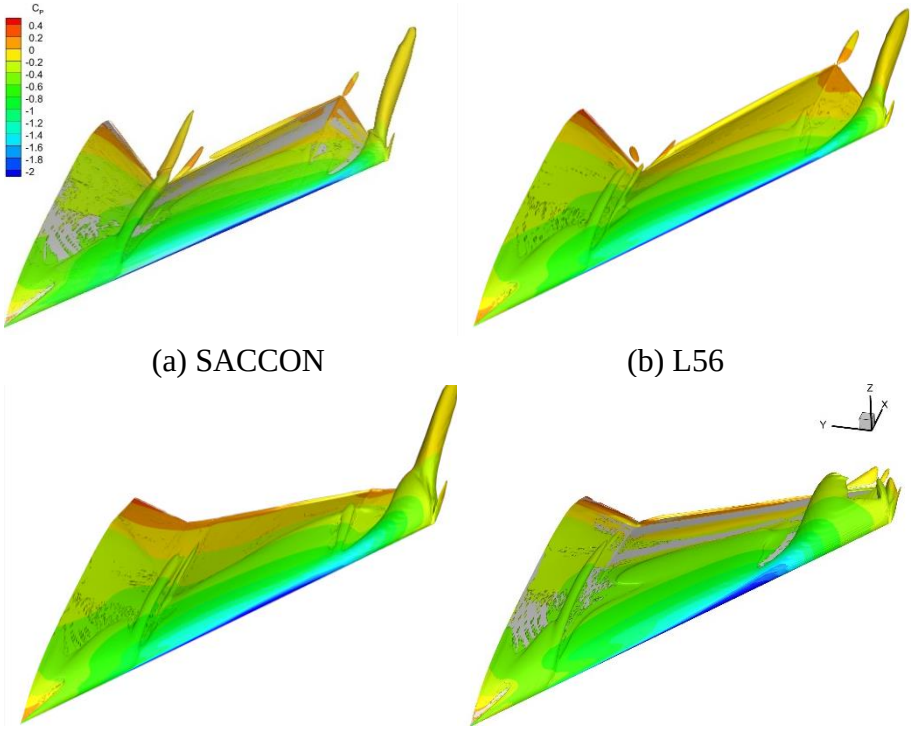
At an angle of attack of 19°, the apex vortex at $x/c_r = 0.2$ intensifies notably, particularly for SACCON, where the suction of the apex vortex is significantly more pronounced than that of the other three configurations. The initiation of the wingtip vortex for SACCON, L56, and L56T25 precedes that of the midsection, resulting in a strong suction effect over the outer wing regions at $x/c_r = 0.45$. In contrast, for the X-45C-like setup, the suction linked to the outer wing vortex is not observable at $x/c_r = 0.45$, likely due to its relatively weaker nature. By $x/c_r = 0.7$, the core of the outer wing vortex has shifted inward by over 400 mm for all designs. While the suction of the inner vortex has dissipated for SACCON, L56, and L56T25, it has intensified for X-45C-like compared to its previous state.

In general, surface pressures of SACCON, L56 and L56T25 vary sharply with rising angle of attack, whereas the X-45C-like model presents mild pressure variations due to the larger leading-edge radii. Its outer wing vortex advances forward slowly, and the leading-edge attached flow area shrinks gently. Notably, the pressure distributions of L56T25 reveal only minor differences from L56, except for the suction peak of the wingtip vortex at $x/c_r = 0.7$. Conversely, the X-45C-like displays a weaker, more inboard apex vortex, lacks outer wing suction at $x/c_r = 0.45$, and consistently exhibits lower leading-edge suction peaks. Thus, leading-edge radii distribution dominates vortex evolution.

3.3 Physical mechanism of the variation of pitch-up characteristics

To show the physical mechanism of the variation of pitch-up characteristics, quantitative analysis based on the λ_2 vortex identification criterion is discussed here. Regions of negative λ_2 values intuitively represent the location and intensity of vortex cores.

The demonstration of the vortex at an angle of attack of 12° is given in Fig. 13. The SACCON contours indicate a relatively weak, confined vortex core structure that is largely limited to a small region near the leading edge. For L56 and L56T25, though the leading-edge radii are the same, the wingtip vortex strength of L56 is nearly the same as SACCON's but weaker than that of L56T25 due to the different pressure gradient near sections C and C'; the apex vortices of both L56 and L56T25 remain weak and do not reach the trailing edge due to a higher leading-edge sweep angle and a smaller normal leading-edge Mach number. By contrast, the X-45C-like configuration shows markedly different behavior over the same angle-of-attack range. Its λ_2 contours reveal a more inboard apex vortex and a stronger wingtip vortex because of the larger leading-edge radius at section B' while a smaller one is present at section C'.

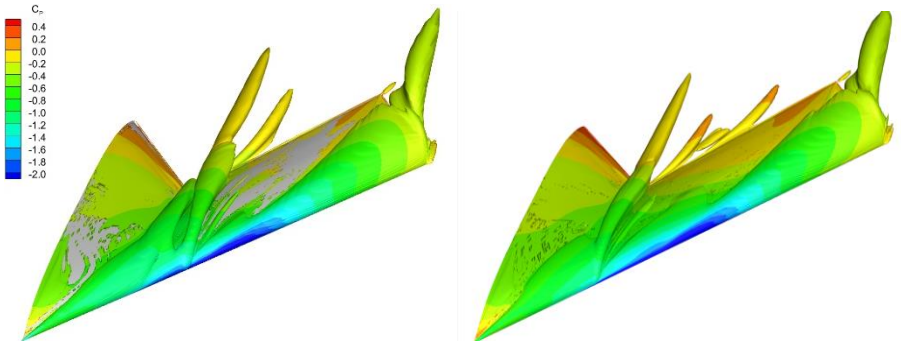


(a) SACCON (b) L56

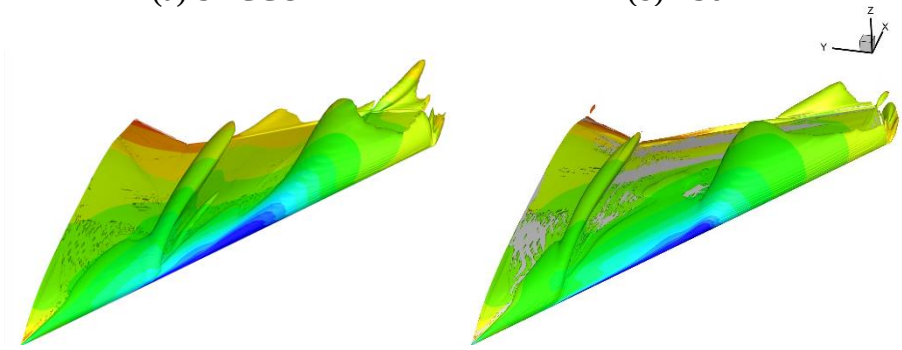
(c) L56T25 (d) X-45C-like

Fig. 13 – λ_2 iso-surfaces ($\lambda_2 = -10^5$), colored by pressure coefficient ($\alpha = 12^\circ$)

The evolving apex and wingtip vortices become intense at an angle of attack of 15°, as shown in Fig. 14. An extra vortex distinctly forms near the leading edge of the inner crank for the SACCON configuration. The pressure contours of L56 are similar to those of SACCON; yet consistent with surface pressure data, only apex and wingtip vortices exist for L56. This demonstrates that vortical flow characteristics are sensitive to the leading-edge sweep angle. Likewise, neither L56T25 nor the X-45C-like configuration generates extra vortices, though their wingtip vortices initiate further forward and influence a broader area. However, the X-45C-like configuration possesses a larger attached-flow zone at the outer wing trailing edge. Its relatively weak apex vortex and insufficient vortex lift on the rear section lead to a much milder change in pitching moment.



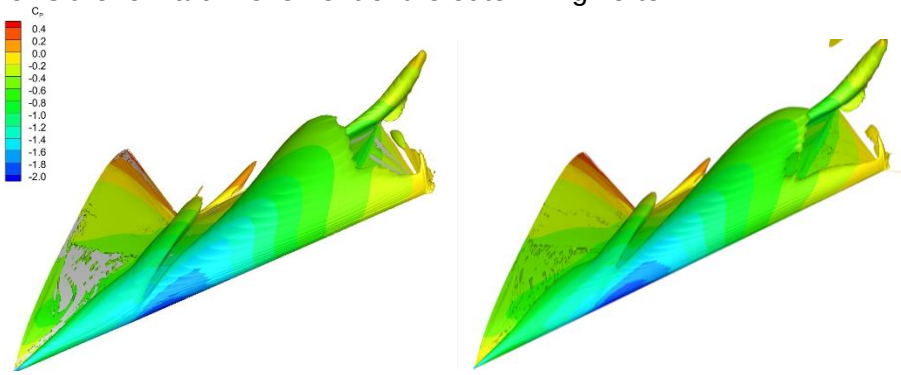
(a) SACCON (b) L56



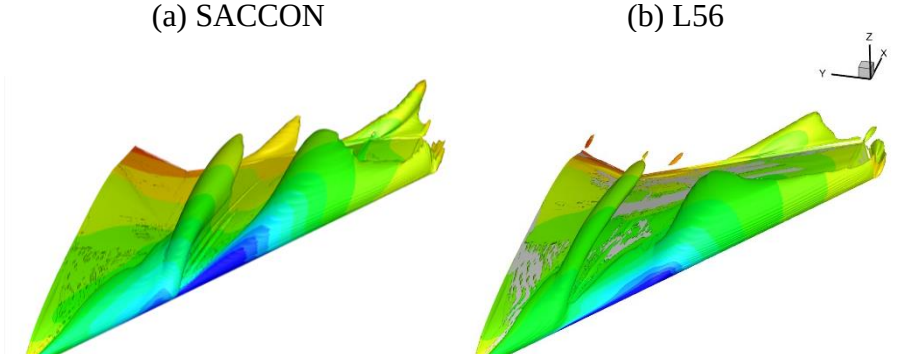
(c) L56T25 (d) X-45C-like

Fig. 14 – λ_2 iso-surfaces ($\lambda_2 = -10^5$), colored by pressure coefficient ($\alpha = 15^\circ$)

As the angle of attack rises to 17°, the vortex systems of the SACCON, L56 and L56T25 configurations grow stronger: vortex cores intensify and expand spanwise and streamwise, while the apex vortex and outer-wing vortex gradually draw closer to each other, as illustrated in Fig. 15. L56T25 features a stronger apex vortex yet a marginally weaker outer-wing vortex. Due to insufficient suction, the inception point of its outer-wing vortex may be shifted further away from the apex vortex. For the X-45C-like model, both the apex and outer-wing vortices remain relatively weak, with a noticeably wide separation maintained between them. This reveals that the increased leading-edge radius at Section B' effectively slows the forward movement of the outer-wing vortex.



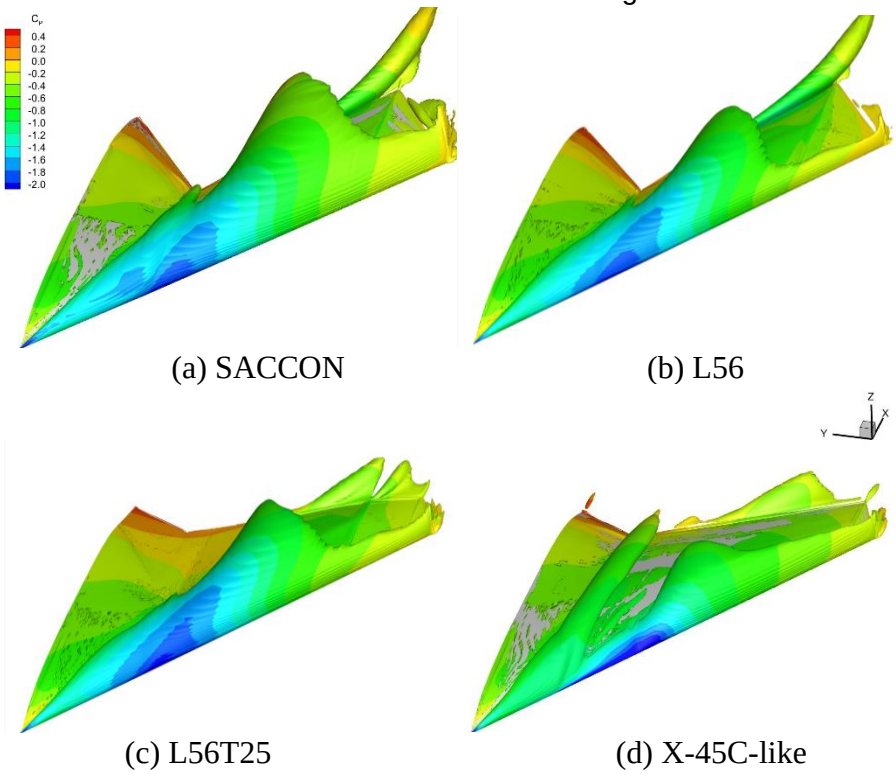
(a) SACCON (b) L56



(c) L56T25 (d) X-45C-like

Fig. 15 – λ_2 iso-surfaces ($\lambda_2 = -10^5$), colored by pressure coefficient ($\alpha = 17^\circ$)

For SACCON, L56 and L56T25, the outer-wing vortex intensifies and eventually coalesces with the apex vortex. A dominant combined vortex structure nearly covering the whole wing forms at 19°, as displayed in Fig. 16. In comparison, vortex strength of the X-45C-like configuration still rises slightly at this angle, yet its outer-wing and apex vortices stay distinctly separated even at 19° angle of attack. Accordingly, enlarging the leading-edge radius at Section B' not only moves the apex vortex further inboard and reduces its intensity, but also greatly restrains the inward shift of the outer-wing vortex, avoiding coalescence into a powerful unified vortex. This accounts for the far gentler pitching moment variation seen on the X-45C-like relative to the other three configurations.



(a) SACCON (b) L56

(c) L56T25 (d) X-45C-like

Fig. 16 – λ_2 iso-surfaces ($\lambda_2 = -10^5$), colored by pressure coefficient ($\alpha = 19^\circ$)

Based on λ_2 vortex analysis, the two configurations exhibit fundamentally different vortex strategies. At angles of attack between 12° and 15°, SACCON and L56 show a weaker, confined wingtip vortex core near the leading edge, aiming to suppress early vortex formation. In contrast, L56T25 and X-45C-like develop intense, extensive wingtip vortices that actively exploit the flow field. Beyond 17°, vortices of SACCON, L56 and L56T25 merge into a single strong pair spanning the wing, while X-45C-like's vortices intensify yet remain distinctly separate even at 19°. Furthermore, through the analysis of the vortices of L56T25 and X-45C-like under the same planform, the larger leading-edge radius distribution on the mid-wing of the X-45C-like is the key factor that suppresses the forward migration of the outer-wing vortex. Thus, SACCON delays and merges vortices, whereas X-45C-like promotes early, sustained, and independent vortex development.

4. Conclusion

Flying-wing configurations are regarded as the preferred configuration for future UCAVs owing to their superior aerodynamic performance and stealth capabilities. Nevertheless, most flying-wing designs adopt moderate aspect ratios and moderate leading-edge sweep angles, and they commonly suffer from nonlinear pitch-up. This undesirable phenomenon severely limits the maximum usable lift coefficient. To investigate the influence of planform and sectional airfoils on moment characteristics, this study examines the aerodynamic features of four flying-wing UCAVs, namely SACCON, L56, L56T25, and X-45C-like, across an angle of attack range of 0° to 19°.

（1） Grid convergence and numerical validation demonstrate that the adopted RANS method with the Spalart–Allmaras turbulence model can reliably predict aerodynamic forces, moments and

overall vortex structures before vortex breakdown. Although minor deviations exist in local pressure distribution and vortex core position at post-stall conditions, the numerical results are sufficiently credible for the present comparative analysis.

（2） Planform exerts a prominent influence on the aerodynamic characteristics and pitch-up behavior of flying-wing UCAVs. With sectional airfoils kept identical, increasing the leading-edge sweep angle (from 53° of SACCON to 56° of L56) effectively delays the onset of pitch-up by approximately 1°. The increased sweep restrains the inboard migration of vortices and weakens the adverse suction effect behind the moment reference point, thus postponing the occurrence of nonlinear pitching moment variation. Under the condition of identical sectional airfoils and leading-edge sweep angles, modifying the aft planform to form the L56T25 configuration cannot eliminate pitch-up completely. Although the abrupt pitch break disappears, the slope of the pitching moment rises obviously starting from around 14°, which is attributed to the rapid forward movement of the outer-wing vortex inception position.

（3） Variations in sectional airfoils and leading-edge radii produce decisive effects on vortex evolution and pitch-up characteristics. The X-45C-like configuration adopts enlarged leading-edge radii, which maintains extensive attached flow on the wing surface, weakens the strength of both apex and outer-wing vortices, and prevents vortex coalescence. This design fundamentally eliminates pitch-up and achieves a maximum usable lift coefficient of 0.8.

（4） The vortex evolution mechanism differs distinctly among the four investigated configurations. For SACCON and L56, the apex vortex and outer-wing vortex gradually approach and eventually merge at high angles of attack, generating strong suction before the moment reference point and triggering pitch-up. In contrast, the X-45C-like configuration maintains a clear separation between the two vortex systems over the full angle-of-attack range, and its mild vortex strength and slow migration speed lead to stable pitching-moment characteristics.

For high-performance flying-wing UCAV design, a simple combination of either planform or sectional airfoil alone cannot fully resolve the pitch-up. Integrated matching design of planform and sectional airfoils (especially leading-edge radii) is essential to balance aerodynamic performance and stealth capability.

5. Copyright Statement

The authors confirm that they, and/or their company or organization, hold copyright on all of the original material included in this paper.

The authors also confirm that they have obtained permission, from the copyright holder of any third party material included in this paper, to publish it as part of their paper. The authors confirm that they give permission, or have obtained permission from the copyright holder of this paper, for the publication and distribution of this paper as part of the ICAS proceedings or as individual off-prints from the proceedings.

References

[1] Garner, H. C., Bouter, M. Z., Chappell, P. D., Dexter, P. C. et al. Effect of Planform Geometry on Low Speed Pitch-break Characteristics of Swept Wings, ESDU 01005, October 2001.

[2] Schütte, A., Hummel, D., Hitzel, S. M. Numerical and Experimental Analyses of the Vortical Flow Around the SACCON Configuration, AIAA Paper 2010-4690, 2010.

[3] Zimper, D., Hummel, D. Analysis of the Transonic Flow Around an Unmanned Combat Aerial Vehicle Configuration, Journal of Aircraft, Vol. 55, No. 2, March-April 2008.

[4] Cummings, R. M., Schütte, A. An Integrated Computational/Experimental Approach to UCAV Stability & Control Estimation: Overview of NATO RTO AVT-161, AIAA Paper 2010-4392, 2010.

[5] Ziper, D., Rein, M. Experimental and Numerical Analysis of the Transonic Vortical Flow over a Generic Lambda Wing Configuration, AIAA Paper 2014-2005, 2014.

[6] Coppin, J., Birch, T. CFD Predictions of Control Effectiveness for a Generic Highly Swept UCAV Configuration, AIAA Paper 2014-2135, 2014.

[7] Nangia, R., Coppin, J., Ghoreyshi, M. UCAV Wing Design, Assessment and Comparisons, AIAA

Paper 2018-2842, 2018.
[8] Nangia, R., Ghoreyshi, M, Rooij, M. P.C., Cummings, R. M. Aerodynamic Design Assessment and Comparisons of the MULDICON UCAV Concept, Aerospace Science and Technology, 93：105321, 2019.
[9] Nangia, R., Boelens, O. J., Tormalm M. A Tale of Two UCAV Wing Designs, AIAA Paper 2010-4397, 2010.
[10] Kügler, Martin E., Florian Holzapfel. Designing Autonomous Flight Capabilities for UAV and OPV–A Comparison of Development and Flight Test Experiences, AIAA Paper 2020-3269, 2020.
[11] Hövelmann, A., Breitsamter. Aerodynamic Characteristics of the SAGITTA Diamond Wing Demonstrator Configuration, Deutsche Gesellschaft für Luft-und Raumfahrt-Lilienthal-Oberth eV, 2013.
[12] Warsop, C., Crowther W. J., Shearwood T. NATO AVT-239: Flight Demonstration of Fluidic Flight Controls on the MAGMA Subscale Demonstrator Aircraft, AIAA Paper 2019-0282, 2019.
[13] Spalart, P. R., Allmaras, S. R. A One-Equation Turbulence Model for Aerodynamic Flows, AIAA Paper 92-439, 1992.
[14] Chakravary, S., Peroomian, O., Sekar, B. Some Internal Flow Applications of a Unified-grid CFD methodology, AIAA Paper 96-2926.
[15] Cummings, R. M., Schütte, A. Integrated Computational/Experimental Approach to Unmanned Combat Air Vehicle Stability and Control Estimation, Journal of Aircraft, Vol. 49, No. 6, 2012.